Journal of *Marine Science and Engineering*

MDPI

*Article*

# Design and Demonstration of an Underwater High-Stability Rapid Cross-Domain Unpowered Vehicle

**Zhiyi Yang [1], Kaiyan Hou [1], Yu Cui [1], Lu Liu [2], Jinglong Wen [1], Haozhe Zhang [1], Zujiang Yuan [1], Dan Liu [1,*] and Chenyang Xue [1]**

[1] State Key Laboratory of Dynamic Measurement Technology, North University of China, Taiyuan 030051, China; yangzhiyi1027@163.com (Z.Y.); bubaihou3@163.com (K.H.); jxzy615727@163.com (Y.C.); 20200002@nuc.edu.cn (J.W.); z18548109632@163.com (H.Z.); 18984519927@163.com (Z.Y.); xuechenyang@nuc.edu.cn (C.X.)

[2] School of Electronic Science and Technology, Xi'an Jiaotong University, Xi'an 710049, China; liulu2235909526@163.com

* Correspondence: liudan235@nuc.edu.cn

**Abstract:** Unpowered vehicles are designed for subaquatic operation and are capable of operating rapidly cross-domain. This paper presents a refined and optimized design for a high-stability rapid cross-domain unpowered vehicle. The use of a compact, uniquely configured gas generator maximizes the rapidity of the ascent phase, achieving an average underwater speed of more than 3.5 m/s, all without the need for an additional propulsion system. To enhance the stability of the unpowered vehicle during the cross-domain phase, a recoil compensation deceleration device (RCDD) was engineered. This device, which uses a combination of springs and electromagnets, significantly increases both the launch capability and the attitude adjustment capability, by 50%. Furthermore, to facilitate rapid launch in real marine environments and investigate the attitudes before and after crossing domains, a rapid cross-domain launch mechanism is introduced. Through multiple sea trials, the results indicate that the unpowered vehicle can complete the launch process within 4 s under sea state 3 conditions. The unpowered vehicle provides an effective solution for rapid cross-domain operation in complex marine environments.

**Keywords:** underwater vehicle; rapid cross-domain; rapid cross-domain motion; ocean environments

check for updates

Academic Editor: Marco Cococcioni

Received: 7 January 2025
Revised: 24 January 2025
Accepted: 30 January 2025
Published: 4 February 2025

**Citation:** Yang, Z.; Hou, K.; Cui, Y.; Liu, L.; Wen, J.; Zhang, H.; Yuan, Z.; Liu, D.; Xue, C. Design and Demonstration of an Underwater High-Stability Rapid Cross-Domain Unpowered Vehicle. *J. Mar. Sci. Eng.* **2025**, *13*, 289. https://doi.org/10.3390/jmse13020289

**Copyright:** © 2025 by the authors. Licensee MDPI, Basel, Switzerland. This article is an open access article distributed under the terms and conditions of the Creative Commons Attribution (CC BY) license (https://creativecommons.org/licenses/by/4.0/).

## 1. Introduction

Cross-domain platforms, as one of the most innovative technological achievements of humanity with far-reaching vision, demonstrate the ability to move within an underwater environment, rapidly transition from the aquatic phase to the aerial realm, and perform specific missions within airspace [1]. Since the conceptualization of submarines by the Danish Navy in the 1930s and the advanced vision of the engineers of the Soviet Union of an amalgamation of the capabilities of aircraft and submarines, embodied in their blueprint for an "underwater airship", the operational platforms for cross-domain applications have evolved from theoretical ideas to practical implementations [2].

In the current technological landscape, unmanned platforms with cross-domain capabilities can be broadly classified into two categories: underwater gliders (UGs) and hybrid aerial underwater vehicles (HAUVs). UGs have shown considerable efficacy, primarily for tasks that are remote and deep-sea and that require extended endurance; however, a rapid transition speed between media is not an inherent strength of UGs [3]. Fixed-wing

aircraft designed for cross-domain operations have exhibited exceptional aerodynamic efficiency and endurance [4], yet these prototypes are subject to stringent requirements in terms of speed and attitude during the critical domain transition phases. Moreover, during the critical cross-domain phase, their sensitivity to surface disturbances increases significantly [5]. Multirotor HAUVs have shown stability during cross-domain travel [6] and have successfully demonstrated comprehensive cross-domain capabilities in real oceanic environments [7]. The use of biomimicry-inspired adaptive propellers has mitigated this impact, allowing for a seamless transition from surface stillness to aerial flight in 0.16 s, although the underwater propulsion efficiency remains low [8]. The TJ-FlyingFish utilizes a transmission mechanism to enable its aerial motor to operate efficiently underwater or employs additional underwater thrusters to enhance its underwater efficiency [9]. To date, the development of HAUVs has primarily focused on establishing the feasibility of their conceptual and theoretical foundations. When considering their underwater operational efficiency, speed, and endurance, HAUVs of any configuration exhibit a three-fold or greater disparity in their aerial operational capabilities compared to those of their equivalent aircraft counterparts [10]. Therefore, integrating platforms across two entirely different media is exceptionally challenging, and the comprehensiveness of HAUVs can actually become a liability.

In light of the underwater operational duration required, we have drawn inspiration from the design principles of a cylinder-launched unmanned aerial vehicle [11]. Using the capabilities of advanced robotic systems [12], coupled with a variety of suitable drone deployment technologies for launch [13–15], and the maturity of vertical launch techniques [16], it is feasible to allow cross-domain platforms to concentrate on underwater operations with optimized efficiency. Furthermore, in the cross-domain phase of the two-phase transition, advances in the study of the hydrodynamic characteristics of the cylindrical bodies that exit the water have facilitated the development of more rapid and energy-efficient control strategies necessary for the cross-domain process [17–19]. This paper provides a comprehensive overview of the design and functionality of a cross-domain vehicle, referred to as an unpowered vehicle. The workflow is illustrated as shown in Figure 1.

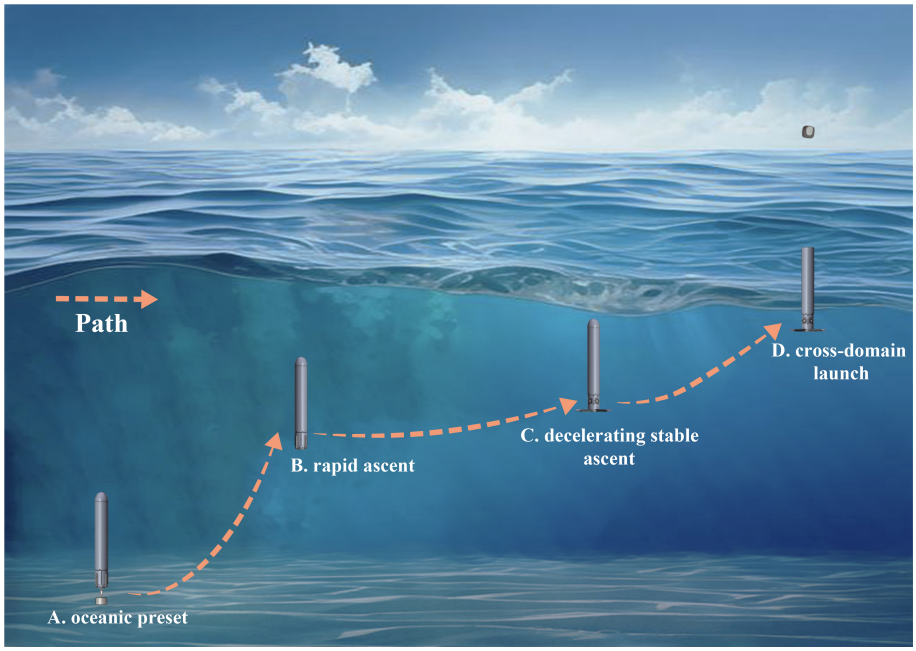



**Figure 1.** Illustration of the workflow diagram.

A combination of aluminum alloy and stainless steel is used in the unpowered vehicle, which offers exceptional resistance to hydrostatic pressure. The target structural weight of the prototype is 28 kg, which has been verified to operate effectively under a water pressure of 1 MPa through testing. This design addresses the current limitations on the underwater working time and the duration of the cross-domain transition in the system by means of comprehensive analysis and experimental validation of the underwater ascent phase, the near-surface cross-domain phase, the and launch phase. This approach enhances the overall cross-domain capability of the unpowered vehicle. It should be noted that to date, there have been no reports of an unpowered vehicle successfully completing this entire operation process in a complex marine environment, with the application of this kind of vehicle mainly concentrated in civil sectors, such as rescue operations. This research presents three major innovative achievements within the cross-domain vehicle as follows.

1. The design of a recoil compensation deceleration device (RCDD) to improve the stability during the cross-domain phase has been both theoretically analyzed and practically tested to address vehicle flooding problems and the insufficient launch altitude during the launch process.
2. To increase the rapidity of cross-domain operations and their robustness in complex environments, a study is conducted on the attitude changes before and after the cross-domain process, with the aim of integrating these findings as an innovative control strategy for the rapid cross-domain launch mechanism.
3. The system has undergone extensive testing across all stages in both real sea and lake environments, demonstrating its repeatability under adverse marine conditions.

The remainder of the article is organized as follows. Section 2 presents the design, electronics, and dynamics of the unpowered vehicle. Section 3 delves into the launch capabilities of the unpowered vehicle, which includes a rapid cross-domain launch mechanism. Section 4 addresses the performance characteristics of the RCDD, including simulation-based analyses and empirical validation. Section 5 demonstrates the vehicle's performance using test results obtained under marine environmental conditions. Section 6 concludes this study.

## 2. The Design and System

### *2.1. Configuration*

The unpowered vehicle has dimensions of 1950 mm in length, 190 mm in width, and 190 mm in height, integrating the ejection component, the unlocking system, and the RCDD. Figure 2a,b illustrates the layout of the design and the key dimensions of the system.

The ejection module assembly is mainly composed of an aluminum alloy tube with a length of 1580 mm, an inner diameter of 160 mm, and an outer diameter of 170 mm, featuring an anodized surface for corrosion resistance. The remainder of the assembly is compactly mounted beneath the vehicle's body. The RCDD is secured to the bottom of the unlocking system via a cylindrical pin, with the recovery and deployment forces imparted separately using an electromagnet and a spring. All of the components are designed for easy disassembly.

The total weight of the unpowered vehicle is 28 kg, with the longitudinal distribution of the weights of the main components shown in Figure 3a. The figure identifies the center of gravity (CG), the center of buoyancy (CB), and the waterline position. As illustrated in Figure 3b, the ejection component represents the highest weight, constituting 48% of the total, followed by the unlocking system, the payload, and the RCDD.

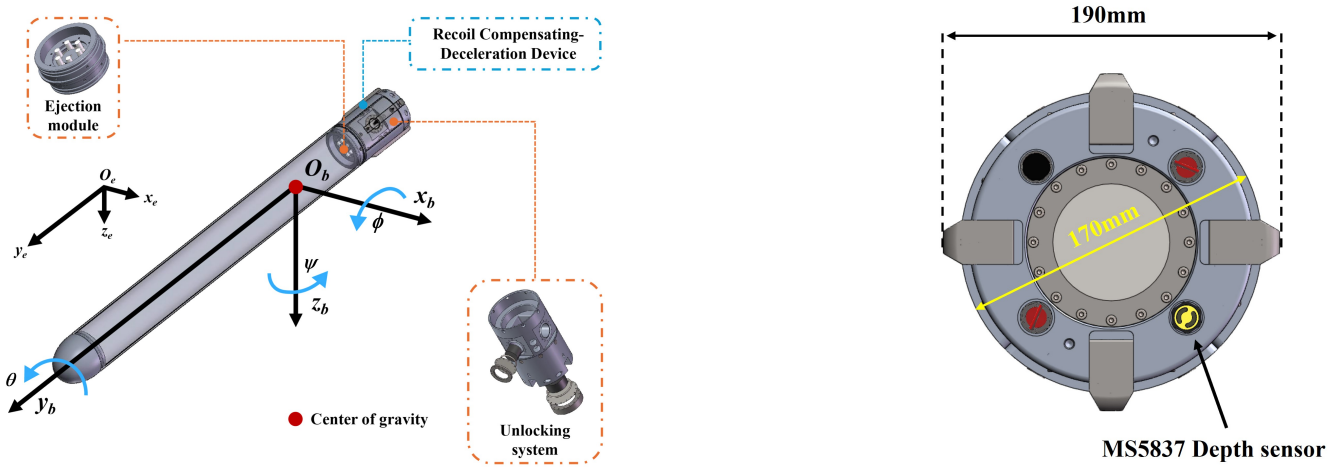



**Figure 2.** The design layout diagram for unpowered vehicle: (**a**) a model diagram featuring annotated coordinate axes. (**b**) Bottom view.

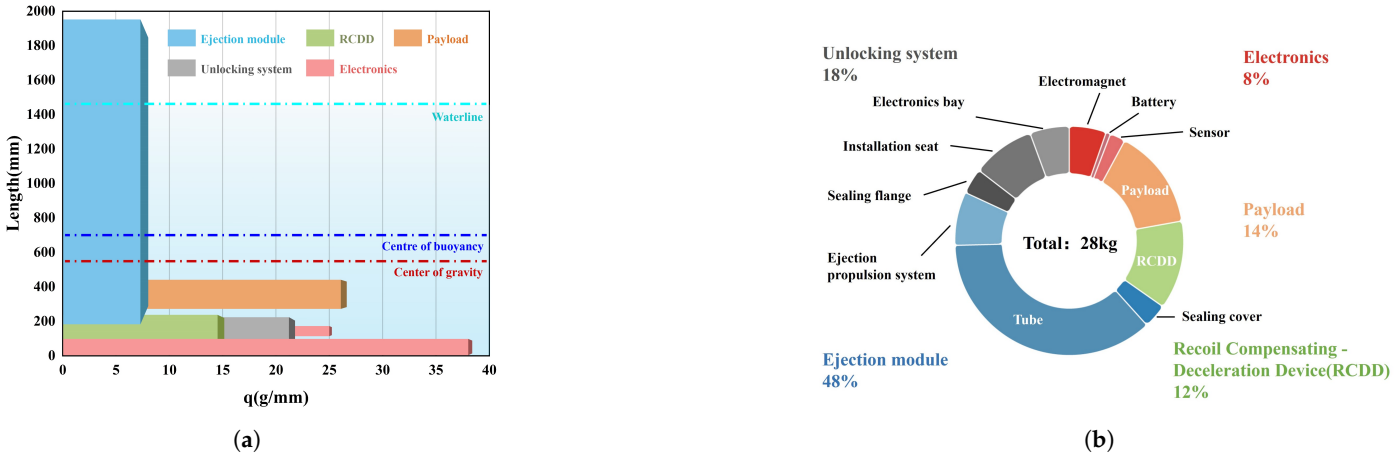



**Figure 3.** Weight information on the unpowered vehicle: (**a**) the diagram of the longitudinal distribution of the weight incorporates the positions of the center of gravity (CG), the center of buoyancy (CB), and the waterline. (**b**) Mass distribution of the unpowered vehicle.

The unpowered vehicle is sealed using a design that incorporates dual O-rings into the piston, thereby ensuring the stability of the internal tube environment. The unlocking system uses a de-energized electromagnetic coil. Although the electromagnetic coil itself has an IP68-level protective performance, its sealing integrity must be considered in the design under deeper and longer-term immersion conditions. To address this, an installation flange design is introduced, which uses thin iron sheets to effectuate both sealing and magnetic flux transfer, thus ensuring the reliability of the unlocking mechanism and its ability to rapidly unlock in complex environments. The limitations on the suction force and distance are as follows:

$$F_e = k \cdot \frac{N_e \cdot I \cdot L_e}{d_e} \tag{1}$$

where, $F_e$ denotes the electromagnetic attraction, $d_e$ represents the distance between the electromagnet and the iron block, $N_e$ is the number of turns in the coil, $I$ is the current flowing through the coil, and $L_e$ is the length of the coil. The constant $k$ pertains to the geometric parameter.

To further elucidate the torque relationship between the spring force and the attractive electromagnetic force, an analytical approach was taken by examining a simplified force diagram of the RCDD, as illustrated in Figure 4. The spring force can be estimated utilizing Hooke's law:

$$F_s = \frac{G_s {d_s}^4 \Delta x}{8nD_s} \tag{2}$$

where $F_s$ signifies the spring's restoring force, and $\Delta x$ denotes the compression of the spring, while $G_s$, $d_s$, $n$, and $D_s$ are the respective parameters characterizing the spring.

$$F_{e1} l_{h2} > F_s l_{h1} \tag{3}$$

Ultimately, considering the compact structural design, the installation volume is a critical factor to meticulously address. Therefore, we selected dimensions of $d_e$ = 0.2 mm, $l_{h1}$ = 174 mm, and $l_{h2}$ = 134 mm. The electromagnetic solenoid for the unlocking component is rated at 40 kg. In the lower unlocking section, to counterbalance the positive buoyancy of 15 kg, a redundant 100 kg electromagnetic element was chosen. All of the components successfully passed static water pressure tests at a pressure of 1 MPa and were substantiated under oceanic conditions at a depth of 50 m.

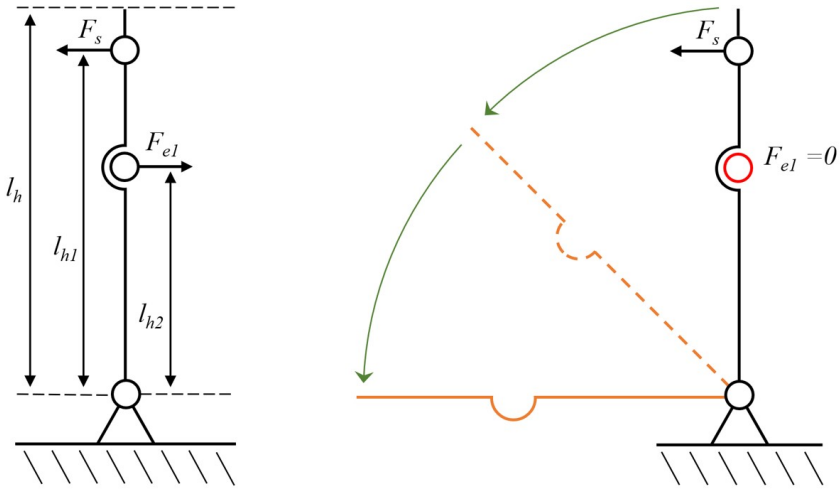



**Figure 4.** Simplified diagram of force distribution in the recovery (**left**) and operational states (**right**) of the RCDD.

### *2.2. Electronics*

The electronic equipment in the unpowered vehicle is housed entirely at the bottom, which requires a sufficiently compact design. Consequently, in the selection of the electronic components, in addition to the power considerations, size also emerged as a critical criterion.

The electronic system of the unpowered vehicle is mainly made up of a power module, a controller, and various sensors. The controller is integrated with an STM32 microcontroller and multiple interfaces. Four relays are connected to the controller GPIO ports, with each controlling the ejection module and the two-part unlocking system. The controller is also connected to independent sensors: depth is measured using a miniature pressure sensor (MS5837), which is verified for a resolution and accuracy of 1 cm, and the Inertial Measurement Unit (IMU) is the HWT605, with an accuracy of 0.05°; the former requires the I2C protocol, while the latter communicates via USART serial ports. Underwater data storage is facilitated by an SD card, which communicates via the SPI protocol. The power supply for the unpowered vehicle is provided by a 1500 mAh 3S Lipo battery. The connections of the components are illustrated in Figure 5, with red representing power

and green representing signals. In this project, the controller was pre-programmed for underwater operation; upon detecting the received depth and attitude data, the controller performs data recording, unlocking, and launch for the unpowered vehicle.

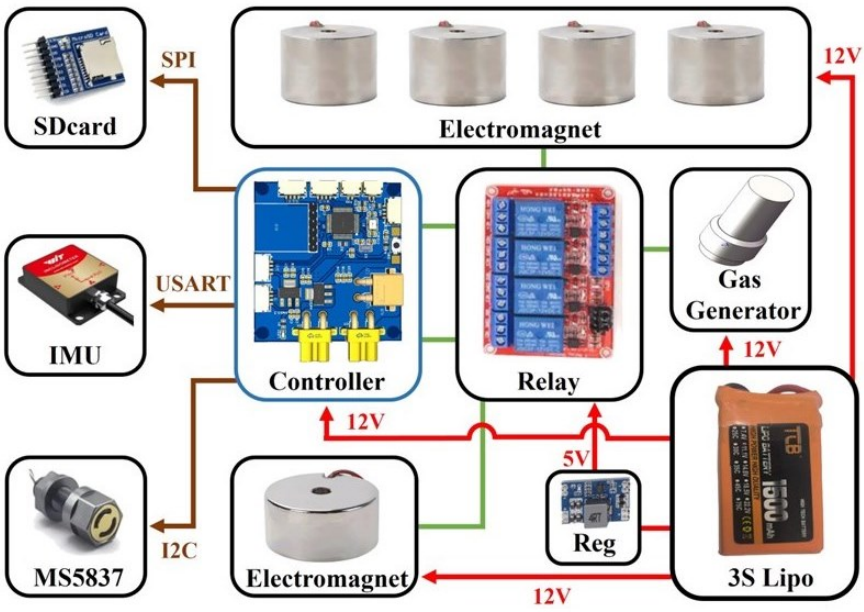



**Figure 5.** Schematic representation of electrical framework.

### 2.3. Dynamics

A geometric model of the unpowered vehicle is illustrated in Figure 2a, which defines two coordinate systems for the analysis: an inertial frame, $\{\mathbf{E}\}(O_e, x_e, y_e, z_e)$, and a body coordinate system, $\{\mathbf{B}\}(O_b, x_b, y_b, z_b)$. $O_b$ is rigidly mounted into the CG. In the set $\{\mathbf{E}\}$, the orientation vector is defined as $\boldsymbol{\xi} = [\boldsymbol{\xi}_1^T, \boldsymbol{\xi}_2^T]^T$, which in the position vector is characterized as $\boldsymbol{\xi_1} = \begin{bmatrix} x & y & z \end{bmatrix}^T$ and in the directional vector is specified as $\boldsymbol{\xi}_2 = \begin{bmatrix} \phi & \theta & \psi \end{bmatrix}^T$. In the context of frame $\{\mathbf{B}\}$, the velocity vector is delineated as vector $\boldsymbol{v} = [v_1^T, v_2^T]^T$. The linear velocity vector, denoted by vector $\boldsymbol{v_1} = \begin{bmatrix} u & v & w \end{bmatrix}^T$, and the angular velocity vector, represented by vector $\boldsymbol{v_2} = \begin{bmatrix} p & q & r \end{bmatrix}^T$, characterize the motion. The transformation $J(\boldsymbol{\xi}_2)$ represents the velocity transformation, while $J_1(\boldsymbol{\xi}_2)$ and $J_2(\boldsymbol{\xi}_2)$ denote the rotation matrices that map vector $\{\mathbf{B}\}$ to vector $\{\mathbf{E}\}$.

$$\mathbf{J}_1(\boldsymbol{\xi}_2) = \begin{bmatrix} c_\psi c_\theta & c_\psi s_\theta s_\phi - s_\psi c_\phi & c_\psi s_\theta c_\phi + s_\psi s_\phi \\ s_\psi c_\theta & s_\psi s_\theta s_\phi + c_\psi c_\phi & s_\psi s_\theta c_\phi - c_\psi s_\phi \\ -s_\theta & c_\theta s_\phi & c_\theta c_\phi \end{bmatrix} \tag{4}$$

$$\mathbf{J}_2(\boldsymbol{\xi}_2) = \begin{bmatrix} 1 & s_\phi t_\theta & c_\phi t_\theta \\ 0 & c_\phi & -s_\phi \\ 0 & s_\phi / c_\theta & c_\phi / c_\theta \end{bmatrix} \tag{5}$$

$$\mathbf{J}(\boldsymbol{\xi}_2) = \begin{bmatrix} \mathbf{J}_1(\boldsymbol{\xi}_2) & \mathbf{0}_{3\times3} \\ \mathbf{0}_{3\times3} & \mathbf{J}_2(\boldsymbol{\xi}_2) \end{bmatrix}_{6\times6} \tag{6}$$

where $c_{(\cdot)}$, $s_{(\cdot)}$, and $t_{(\cdot)}$ denote $cos_{(\cdot)}$, $sin_{(\cdot)}$, and $tan_{(\cdot)}$ respectively. The kinematic equations may be expressed as follows:

$$\dot{\boldsymbol{\xi}} = \mathbf{J}(\boldsymbol{\xi}_2)\boldsymbol{v} \tag{7}$$

The dynamical equations [20] can be formulated as follows:

$$\mathbf{M}\dot{v} + \mathbf{C}(v)v + \mathbf{D}(v)v + \mathbf{g}(\eta) = \mathbf{w} \tag{8}$$

where $M \in \mathbb{R}^{6\times6}$ represents the inertia matrix associated with the added mass of fluid dynamics. $\mathbf{C}(v) \in \mathbb{R}^{6\times6}$ is the Coriolis and centripetal matrix. $\mathbf{D}(v) \in \mathbb{R}^{6\times6}$ represents the term resulting from the resistive forces. $\mathbf{g}(\eta) \in \mathbb{R}^6$ contains the restoring terms formed by the vehicle's buoyancy and gravitational terms. $\mathbf{w} \in \mathbb{R}^6$ denotes the environmental forces and torques acting upon the vehicle.

## 3. Launch Capability

### *3.1. The Propulsion Source Test*

In conventional catapult systems, the ejection mechanism is facilitated by the energy provided through auxiliary gas cylinders or pyrotechnics. However, to broaden the applicability of an unpowered vehicle to a wider range of applications, considerations of its safety and ease of use are of paramount importance. In accordance with the dimension limitations and the reduced-center-of-gravity requirements relevant to an unpowered vehicle, our research team conducted a rigorous examination and evaluation of a compact gas generator. The innovation advantage is the pronounced reduction in the volume of the deployment, increasing the portability and maneuverability of the system [11]. Subsequently, the following, Table 1, synthesizes a comparative summary of the principal characteristics of three prevalent ejection sources, encompassing their operational principles [21], spatial dimensions, and regulatory mechanisms [22]. The analytical juxtaposition elucidates the inherent potential and the distinct advantages endowed by the miniaturized gas generator, especially in satisfying customized launch requirements.

**Table 1.** Comparison of performance parameters of centralized launch propulsion sources.

| Characteristics | Electromagnetic Launch | Gas Bottle | Gas Generator |
|---|---|---|---|
| Principles | Lorentz force | Gas pressure | Gas pressure |
| Volume | 0.26 L | 0.22 L | 0.0065 L |
| Control Methods | High voltage | Electromagnetic valve | 3S Lipo |

Based on the relevant data on the launch altitude, an approximate estimate of the initial velocity acquired by the equivalent load of the launch tube can be achieved. During the ejection operation, the primary type of resistance encountered by the equivalent load is attributed to the frictional force exerted by the inner wall of the launch tube [23], and the motion equation for the equivalent load within the unpowered vehicle is given as follows:

$$(P_h - P_0)2\pi r_l(r_l + l) = M_0\frac{dv_p}{dt} + f_p M_0 g \tag{9}$$

where $P_0$ denotes the air pressure, $r_l$ signifies the inner diameter of the launch tube, $l$ represents the length of the launch tube, $M_0$ denotes the total mass, $v_p$ is the velocity of the payload, and $f_p$ corresponds to the frictional force within the tube.

The experiments were carried out using the local atmospheric pressure value of 909 mbar from the test day, with equivalent loads ranging from 2 to 6 kg. The results are presented in Figure 6. The experiments were carried out using a launch tube with a length of 1580 mm. The data charts presented in the results provide a detailed depiction of the heights achieved during the ejection tests under the actual testing conditions, using between three and six gas generators for equivalent loads of various masses (2–6 kg). To

ensure the reference value of the experiments, subsequent trials were conducted using the gas generator quantity and payload weight at point A.

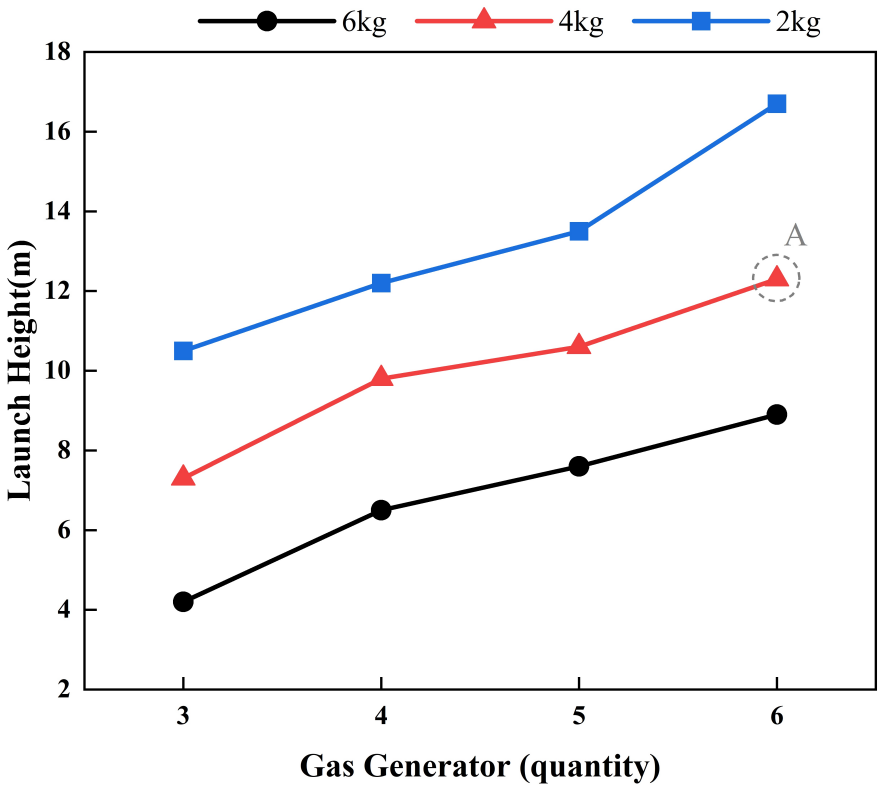



**Figure 6.** Test diagram for the number of gas generators, payload weight, and launch height.

### *3.2. The Rapid Cross-Domain Launch Mechanism*

Given the three orders of magnitude difference in density and viscosity between air and water, the hydrodynamic forces that act on the unpowered vehicle exhibit significant fluctuations during the crossover phase. Consequently, the implementation of a rapid cross-domain launch mechanism is of critical importance tp the unpowered vehicle's ability to rapidly and safely launch the payload to the designated location, thereby ensuring successful completion of the mission.

In contrast to conventional underwater robot control systems that predominantly rely on depth sensors and IMUs, achieving the desired pitch angle to facilitate the ascent and descent of an underwater robot requires the precise control of these vertical movements [24]. This is accomplished by integrating depth and pitch information to obtain the subsequent propeller velocities, ensuring accurate control over the buoyancy of the robot. To meet higher response speeds, an increase in the system's overshoot can lead to instability, necessitating a careful balance to maintain robust control without compromising performance.

During the launch phase of the unpowered vehicle, it is inevitable that the vehicle will be subjected to wave disturbances. Therefore, in addition to the rapidity of the action, the stability of the launch must also be considered. The prerequisite for executing the ejection maneuver stably is stable floating on the water's surface. Upon this foundation, the control module evaluates the desired attitude angle and issues command signals for precise ejection. Here, $E$ represents the desired value, and $T$ represents the measured value. These symbols $E_d$, $E_\psi$, and $E_\phi$ correspond to the expected information for depth and attitude, respectively, with $T_d$, $T_\psi$, and $T_\phi$ being the corresponding measured values. The

system introduces a specified range to apply amplitude constraints to the system variables involved in the calculation.

The launch action is executed when the depth test value $T_d$ is less than or equal to the expected depth $E_d$ for stable floating on the water surface and when $T_\psi$ and $T_\phi$ are also within the respective boundaries $\delta$ of the expected values. This approach alleviates the computational load, enhances the system's rapid response capability, and preserves the integrity of its dynamic stability. The control strategy is illustrated in the flow chart in Figure 7.

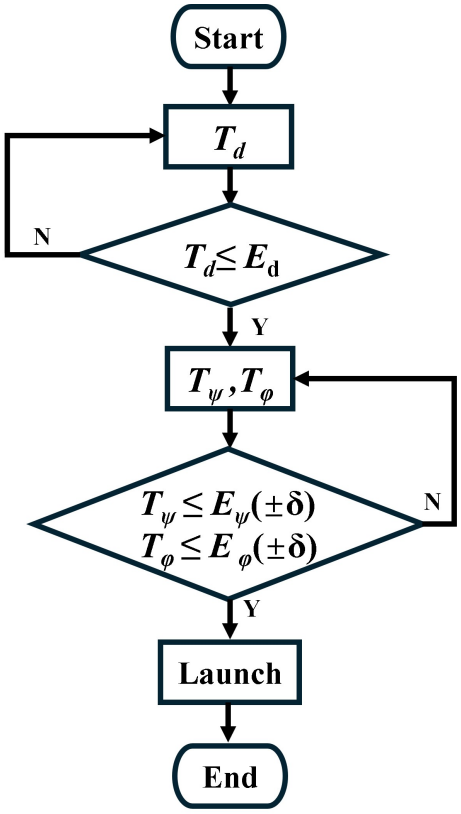



**Figure 7.** Rapid cross-domain launch mechanism control strategy.

## 4. The Recoil-Compensating Deceleration Device

### *4.1. Structural Design*

Under ideal conditions, the unpowered vehicle possesses a sufficient underwater velocity, allowing it to carry out its action at the precise moment when it emerges from the surface of the water, thus ensuring both rapidity and stealthiness of the execution of the mission. However, in practical scenarios, because the underwater velocity is contingent upon the vehicle's adequate positive buoyancy, excessive speed and the cross-domain phase are subject to significant fluctuations. This is mainly attributed to the abrupt change in the fluid medium during the cross-domain process.

This paper presents a recoil-compensating deceleration device (RCDD), and the installation of this type of part is illustrated in Figure 8d. The vehicle is equipped with a total of four RCDDs. These are deployed underwater through the use of four evenly distributed electromagnets and springs, obviating the need for space-consuming mechanisms such as crank-and-slide and multi-link systems. Additionally, to mitigate the errors in shaft hole fitting encountered in practical engineering, a rotatable spherical surface is designed as the unlocking spherical iron column, which is connected to the arm via a ball head bolt.

RCDDs can self-deploy at a 90° angle and can be fully retracted to the vehicle's sides, thus improving their dynamic performance in fluid, as shown in Figure 8a.

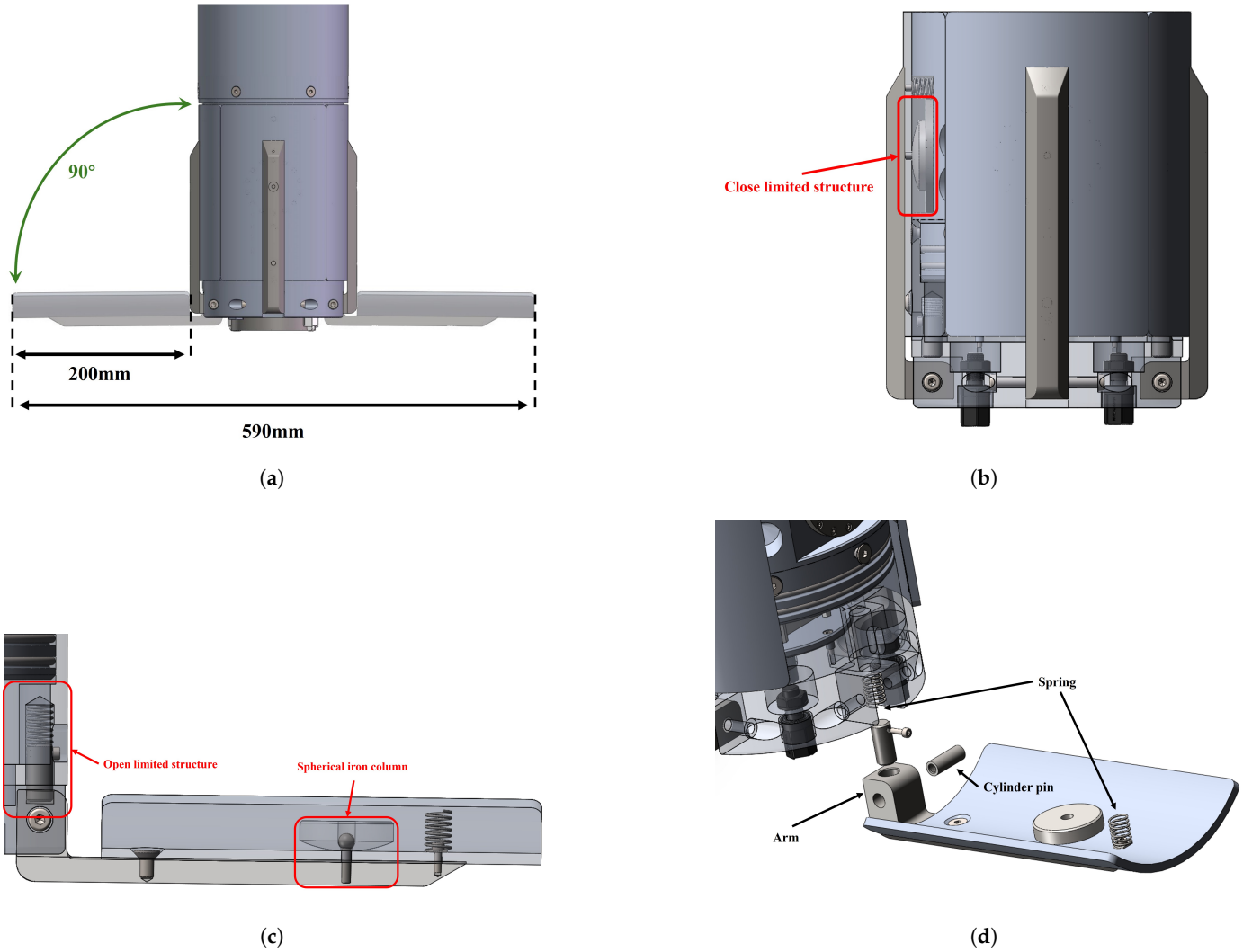



**Figure 8.** Illustrative diagram of the RCDD work process: (**a**) operational state. (**b**) Recovery state. (**c**) Limited structure and spherical iron column. (**d**) Installation diagram.

Two operational modes are demonstrated. Figure 8b illustrates the stages on the seabed and during the acceleration phase of upward ascent. The entire RCDD is constrained by a tightly limited structure, which ensures its operation in the optimal position to maximize the velocity of the unpowered vehicle. Upon the execution of the deployment action, the electromagnets within the closed-loop structure are energized and demagnetized. Under the influence of two compression springs, the arm rotates around the cylinder pin by 90°, ensuring that the RCDD is positioned at a 90° angle relative to the vehicle's axis. This arrangement guarantees the effectiveness of the deceleration and recoil compensation, as shown in Figure 8c.

### *4.2. Simulations and Experiments*

The static restoring moment experienced by an unpowered vehicle during launch while it floats on the water surface is influenced not only by disturbances such as sea breeze and waves but also by its emergence posture. This static restoring moment can be expressed as follows:

As depicted in Figure 9, enhanced stability is attributed to a large value $\overline{GM}$. Upon the complete deployment of the RCDD, the vehicle's CG is significantly lowered, leading to an increase in the restoring moment. This increase in the restoring moment consequently strengthens the overall stability of the vehicle.

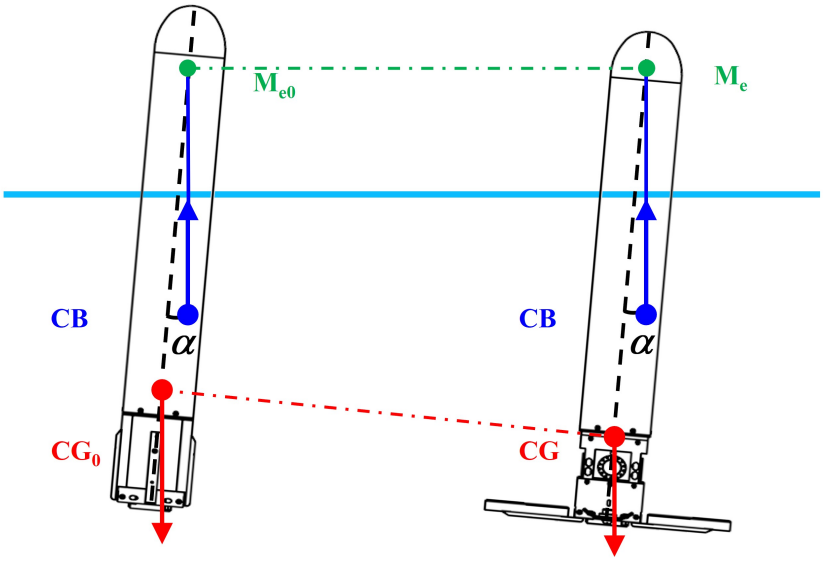



**Figure 9.** Comparison chart of centroid stability between the recycled and operational states of the RCDD.

The unpowered vehicle model was simplified to facilitate a computational fluid dynamics (CFD) analysis, as depicted in the figure. The model omits irregular structures, such as the RCDD, to prevent any potential impact on the accuracy of the grid.

The simulation of wave-based phenomena was conducted using a fifth-order VOF (Volume of Fluid) wave model [25]. The free surface was captured using the VOF method, and the turbulent flow was modeled using the $k-\varepsilon$ model for the simulation setup, solution calculation, and post-processing [26]. The computational domain had dimensions of 135 m in length, 8 m in width, and 10 m in height. A simulation was performed with a prediction that spanned a physical time duration of 20 s. As shown in Figure 10, the instantaneous wave profiles correspond to the peak (Figure 10a) and the trough (Figure 10b) of the heave motion, while the volume fraction graphs represent the wave crests (Figure 10c) and troughs (Figure 10d) corresponding to the attitude angle.

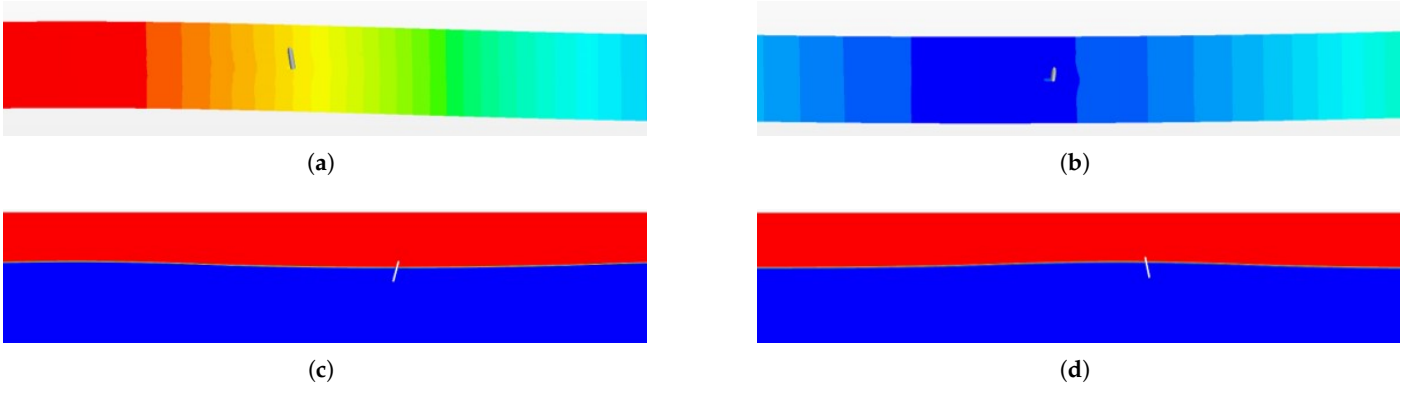



**Figure 10.** Results from CFD simulation: (**a**) maximum heave moment. (**b**) Minimum heave moment. (**c**) $\phi$ peak wave moment. (**d**) $\phi$ trough moment.

Figure 11a,b present a comparison between the numerical results for the unpowered vehicle and the experimental results under a wave condition of 0.5 m. The peak amplitude of the heave motion is close to the measured results, while the peak amplitude of $\phi$ exhibits an error of approximately 10% with respect to the test data. In terms of the trend in the curves, the general trends are consistent with the test results. However, within the same time frame, the wave frequency in the numerical simulation is higher than that observed in the numerical simulation. These results indicate that despite the discrepancy between the measured data and the expected outcomes, the unpowered vehicle is capable of operating effectively under wave conditions of 0.5 m.

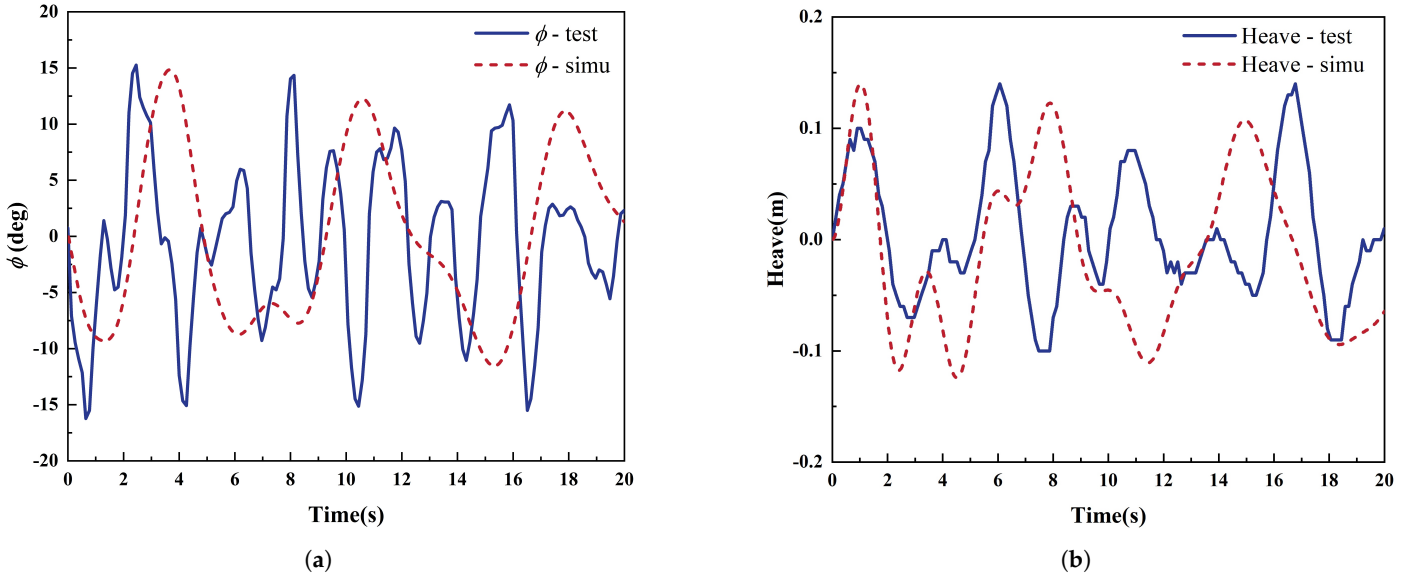



**Figure 11.** Comparison between simulation and experimental data: (**a**) comparison of $\phi$ and (**b**) comparison of heave.

### *4.3. Performance Analysis*

To ascertain the operational performance of the RCDD in real-world conditions, comparative assessments and tests were carried out during the ascent phase in a genuine marine environment. The intervention of the RCDD significantly reduced the time required to stably adjust to the water's surface attitude. As shown in Figure 12, in the absence of the RCDD, the vehicle took 7.72 s of the duration of its appearance above the water's surface (T = 5.29 s) to achieve stable floating on the water's surface (T = 13.01 s). As shown in Figure 13, in an environment nearly identical to the one with the RCDD involved, the unpowered vehicle achieved stable floating on the water's surface in a time span of 5.03 to 6.58 s, requiring only 1.55 s, which represents a reduction of almost 80%. The results of these tests are illustrated in Figure 14.

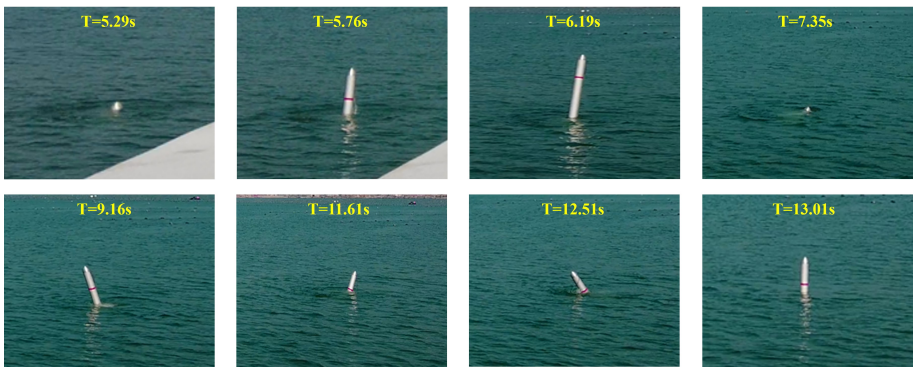



**Figure 12.** Experimental demonstration of attitude adjustment on sea surface (no RCDD involvement).

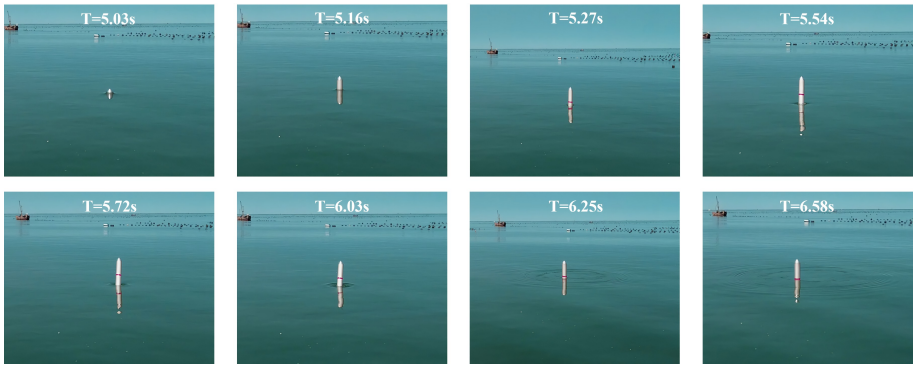



**Figure 13.** Experimental demonstration of attitude adjustment on sea surface (RCDD involvement).

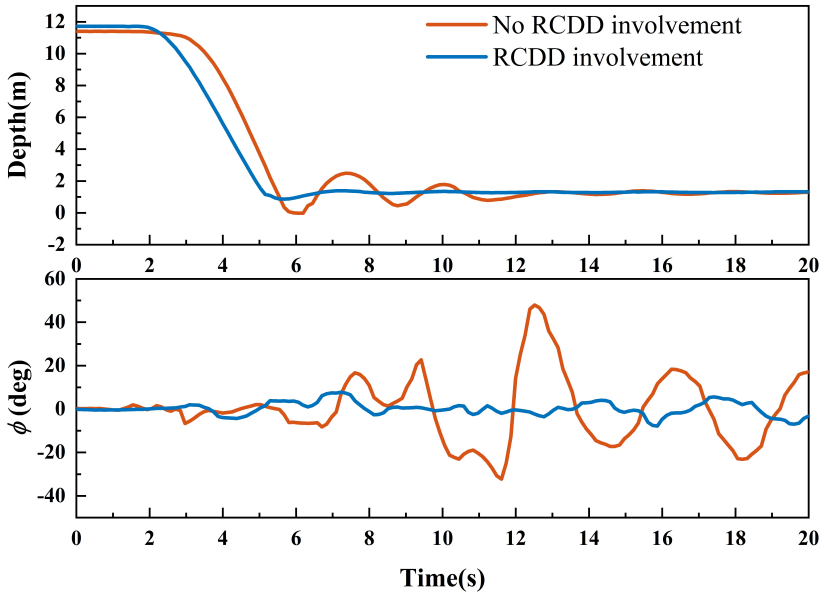



**Figure 14.** Experimental testing in oceanic environments for the RCDD.

In terms of launch capabilities, the main focus was on the compensation for the unpowered vehicle. An experimental investigation into the influence of the RCDD on the launch process was conducted on the surface of a calm lake. A flat, sealed cover was employed to facilitate observation of the vehicle's emergence above the water level and the variation in its height during the launch.

The experiment documented the height variations at equal time intervals of 0.1 s. The video screenshot above illustrates a scenario in which the RCDD is not involved, whereas the one below depicts the data for the participation of the RCDD. The experimental results are presented in Figures 15 and 16. At T = 2.65 s, the unpowered vehicle was fully submerged beneath the water's surface. In contrast, at T = 2.45 s, the unpowered vehicle still maintained a clearance of approximately 20 cm above the water, indicating an improvement in the recoil compensation capacity of approximately 50% (Figure 17). Furthermore, in terms of the launch altitude aspect, the inclusion of the RCDD resulted in a nearly doubling of the launch altitude. The results of the altitude test are illustrated in Figure 18 provided.




**Figure 15.** Experimental testing in oceanic environments for the RCDD.

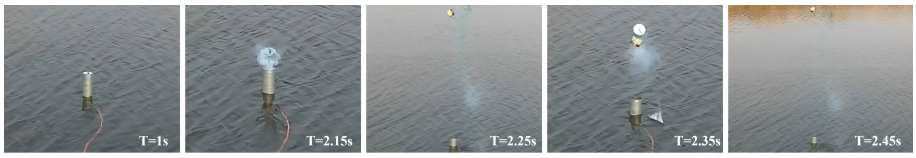



**Figure 16.** Experimental testing in oceanic environments for the RCDD.

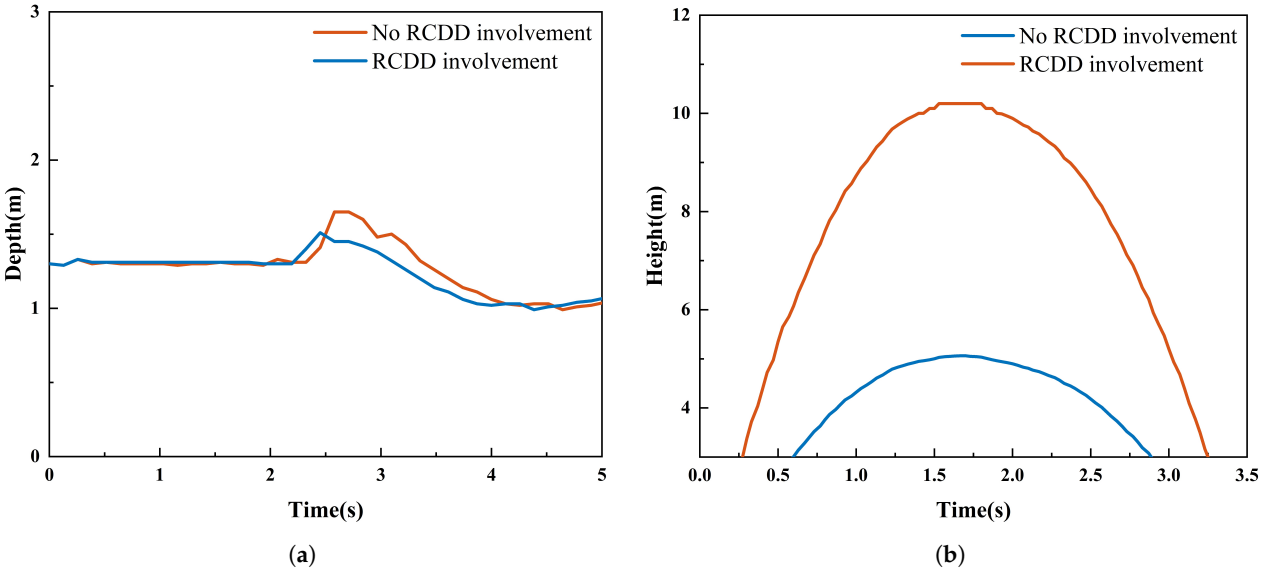



**Figure 17.** Comparison of launch capabilities: (**a**) launch compensation depth. (**b**) Launch height.

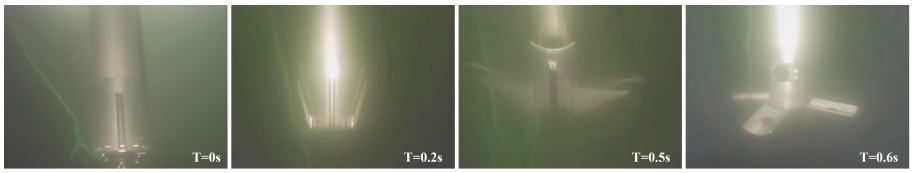



**Figure 18.** Demonstration of RCDD deployment in laboratory water pool.

In order to investigate and analyze the results of the aforementioned experiments, due to the constraints imposed by underwater filming conditions, photographs of the moment at which the RCDD was deployed were captured in a laboratory water pool, as depicted in Figure 18. These images were provided only for illustrative purposes and did not influence the results of the marine and lake tests. The RCDD achieves full deployment in 0.6 s. During the process of adjusting its posture at the water surface, the RCDD unfolds at a pre-set depth, which inevitably reduces the velocity of the unpowered vehicle underwater. During the launch phase, upon deployment, the RCDD increases its contact area with water, as estimated in Section 4.1, by approximately five times. However, the device's intervention notably enhanced the stability of the unpowered vehicle on the water's surface, thereby significantly reducing the overall duration of the cross-domain phase.

## 5. The Sea Trial

To validate our concept, several tests were carried out. The prototype was subjected to field trials in Yantai, Shandong, where the feasibility of the proposed unpowered vehicle was confirmed. Full-process tests under harsh natural conditions further demonstrated the rapid cross-domain capabilities of the unpowered vehicle.

### 5.1. Subaquatic Operations and Performance

The entire buoyant ascent phase of the unpowered vehicle encompasses the initiation of the ascent signal, the activation of the RCDD near the surface, and its stabilization on the water's surface. The experiments were carried out in an oceanic environment with a maximum depth of 50 m. The primary objective of this study was to quantify the submersible operational capabilities of the unpowered vehicle. The experiment primarily measured the attitude and velocity of the vehicle. The acquisition of these data relied on the collaborative functioning of the IMU and the MS5837 sensor.

As depicted in Figure 19, the data on the attitude and depth variations during two upward surfacing processes are presented in waters with a maximum depth of 50 m. The vehicle states were measured at a sampling time of 0.128 s. The uniform change in depth ensures that the trends in the data collected at various depths are consistent, thus yielding higher-quality observational results. Consequently, this study estimates the vertical velocity of the unpowered vehicle by calculating the difference between consecutive depth measurements. The results of the two tests indicate that the maximum underwater velocity exceeded 4.5 m/s, and the average underwater velocity of the unpowered vehicle at a depth of 50 m was greater than 3.5 m/s.

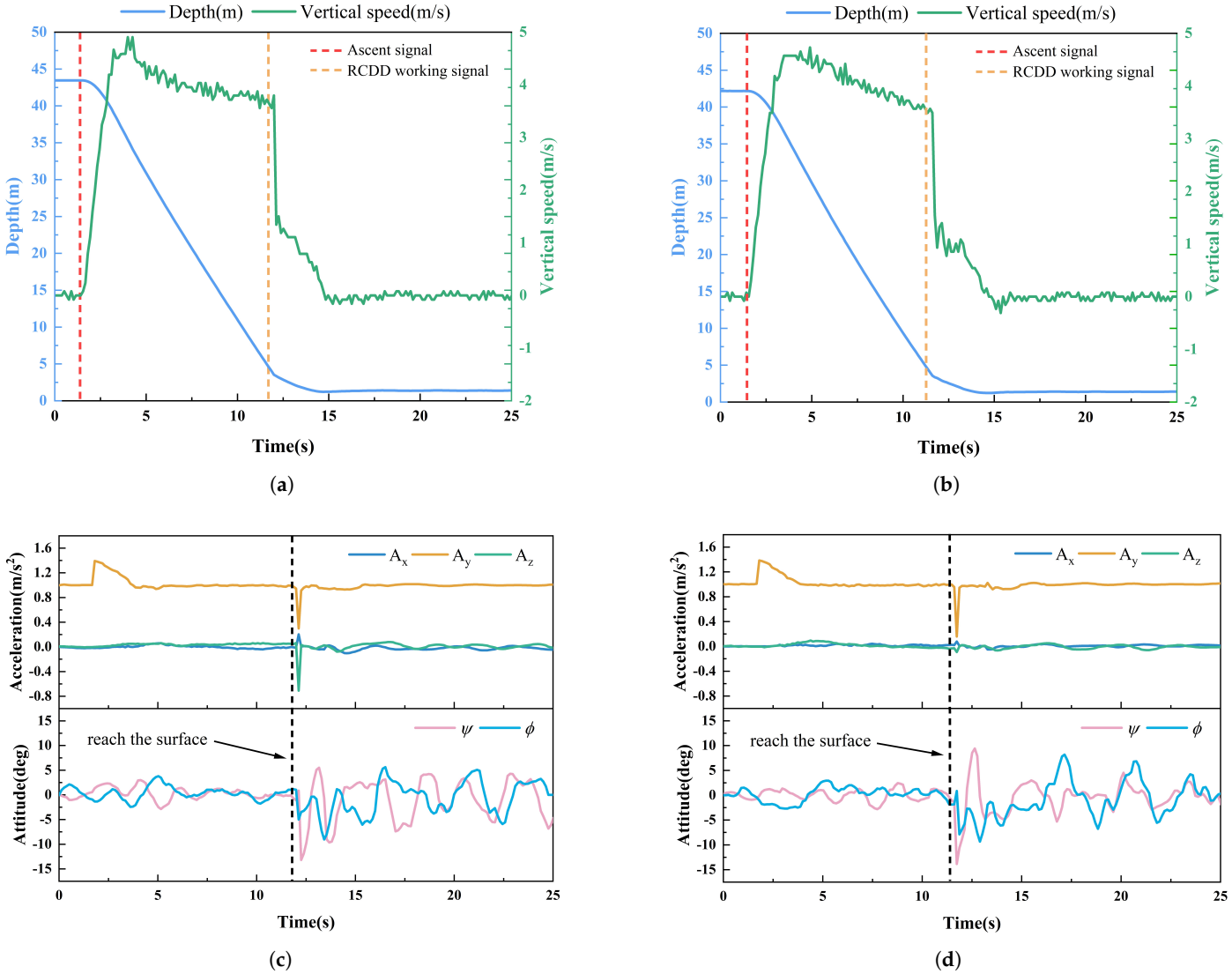



**Figure 19.** Subaquatic test: (**a**,**c**) a set of test data was obtained. (**b**,**d**) An additional batch of test data was obtained.

Within the scope of this research, the velocity data serve predominantly to evaluate the kinematic properties of the unpowered vehicle's buoyancy motion rather than to provide information on the feedback loops integral to operations such as launching. Although the IMU system exhibits inherent limitations in its velocity measurement accuracy, its high-precision capabilities in attitude determination offer a dependable foundation for the activation of a rapid cross-domain launch mechanism. Consequently, the cross-domain mechanism formulated in this study is predominantly contingent upon the unpowered vehicle's attitude parameters rather than velocity-related data.

### *5.2. The Full Process of Rapid Cross-Domain Movement*

In the present study, the cross-domain launch task was meticulously divided into three pivotal phases: the initial ascent phase, followed by the cross-domain phase, and finally the launch phase. Through the experimental evaluation of the ascent phase, it was observed that the ascent processes at various depths exhibited similar regular trends. To ensure the completeness of the experiments, the analysis of the cross-domain phase and the launch phase was based on the data obtained from the ascent testing at different depths. During the cross-domain launch phase, an empirical test was performed on the trigger mechanism and its applicability, as proposed in Section 3.2.

In our systematic testing of the cross-domain capabilities of the unpowered vehicle in both calm and sea state 3 conditions, we conducted experiments in both tranquil and severe weather scenarios. As depicted in Figure 20, in calm weather conditions, the experimental results indicate that the unpowered vehicle can complete the ejection process in 2.8 s (Figure 20a). In severe weather conditions with wave heights greater than 0.5 m (Figure 20b), the ejection and take-off process can be successfully completed in 3.9 s. Figure 21a illustrates the time from the launch point to the highest point in calm waters, while Figure 21b shows the corresponding content under sea state 3 conditions. The calculated weight of the ejection payload is 4 kg, with estimated heights of 9.6 m and 7.8 m, respectively.

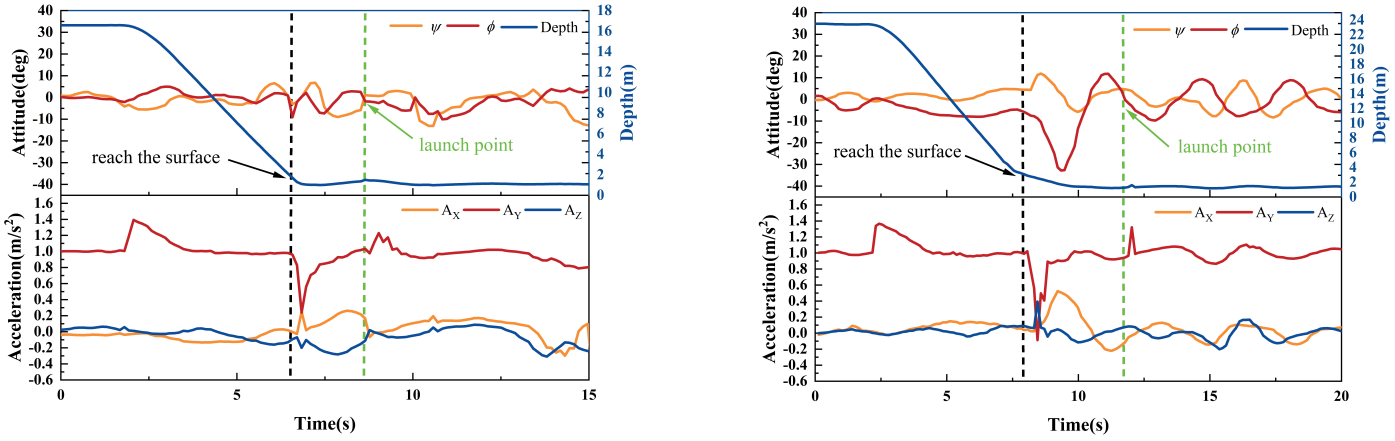
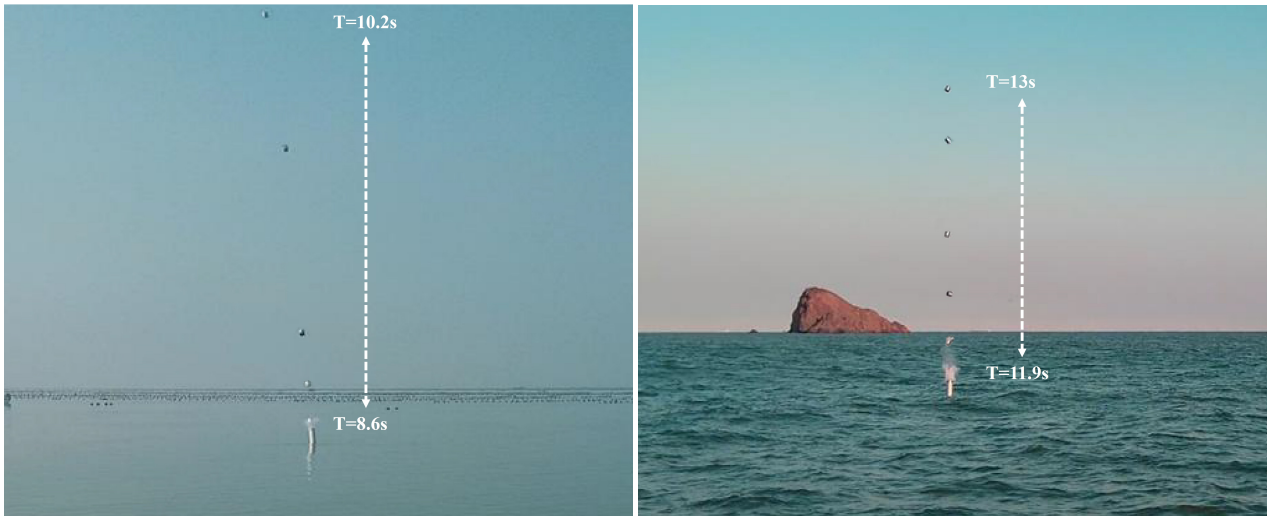



**Figure 20.** Full-process rapid cross-domain test: (**a**) calm sea conditions. (**b**) Sea state 3 conditions.




(**a**) (**b**)

**Figure 21.** Launch altitude time series: (**a**) wurface launch under calm sea conditions. (**b**) Surface launch under sea state 3 conditions.

## 6. Conclusions

This paper presents the improved and optimized design of a high-stability rapid cross-domain unpowered vehicle. During the underwater ascent phase, a distinctive design coupled with a compact gas generator has achieved an average underwater speed of more than 3.5 m/s, all without the need for an auxiliary propulsion system. In the near-surface cross-domain phase, an RCDD has been engineered for enhanced overall cross-domain stability. During the launch phase, the ejection maneuver was accomplished within merely 4 s under sea state 3 conditions. A comprehensive analysis of the ascending motion process and experimental validation have been performed under adverse sea conditions in comparison to the state of the current system. The next objective for this unpowered vehicle involves the development of capabilities to deploy UAVs in the challenging conditions of complex marine environments. We are steadfast in our belief that this unpowered vehicle will instigate a cascade of pivotal applications across the spectrum of oceanographic research, maritime surveillance, and coastal rescue operations.

**Author Contributions:** Conceptualization: Z.Y. (Zhiyi Yang) and D.L. Methodology: Z.Y. (Zhiyi Yang), J.W., and K.H. Software: K.H. Validation: Y.C. and J.W. Formal analysis: Z.Y. (Zujiang Yuan) and L.L. Investigation: Z.Y. (Zujiang Yuan) Resources: D.L. Data curation: K.H. Writing—original draft preparation: Z.Y. (Zhiyi Yang) Writing—review and editing: L.L. and C.X. Visualization: H.Z. Supervision: L.L. and C.X. Project administration: D.L. and C.X. Funding acquisition: D.L. and C.X. All authors have read and agreed to the published version of the manuscript.

**Funding:** This research was funded by the National Natural Science Foundation of China under Grant 62371425; the Special Fund for Science and Technology Innovation Teams of Shanxi Province under Grant 202304051001030; the Shanxi Scholarship Council of China under Grant 2022-144; the Fundamental Research Program of Shanxi Province under Grant 202303021222119; and the 19th Graduate Student Scientific Research Project of North University of China under Grant 20231970.

**Institutional Review Board Statement:** Not applicable.

**Informed Consent Statement:** Not applicable.

**Data Availability Statement:** The data presented in this study are available on request from the corresponding author.

**Conflicts of Interest:** The authors declare no conflicts of interest.

## References


1. Yang, X.; Wang, T.; Liang, J.; Yao, G.; Liu, M. Survey on the novel hybrid aquatic–aerial amphibious aircraft: Aquatic unmanned aerial vehicle (AquaUAV). *Prog. Aerosp. Sci.* **2015**, *74*, 131–151. [CrossRef]
2. Mercado, D.; Maia, M.; Diez, F.J. Aerial-Underwater Systems, a New Paradigm in Unmanned Vehicles. *J. Intell. Robot. Syst.* **2019**, *95*, 229–238. [CrossRef]
3. Yang, M.; Wang, Y.; Liang, Y.; Wang, C. A New Approach to System Design Optimization of Underwater Gliders. *IEEE/ASME Trans. Mech.* **2022**, *27*, 3494–3505. [CrossRef]
4. Wei, T.; Lu, D.; Zeng, Z.; Lian, L. Trans-Media Kinematic Stability Analysis for Hybrid Unmanned Aerial Underwater Vehicle. *J. Mar. Sci. Eng.* **2022**, *10*, 275. [CrossRef]
5. Stewart, W.; Weisler, W.; MacLeod, M.; Powers, T.; Defreitas, A.; Gritter, R.; Anderson, M.; Peters, K.; Gopalarathnam, A.; Bryant, M. Design and demonstration of a seabird-inspired fixed-wing hybrid UAV-UUV system. *Bioinspir. Biomim.* **2018**, *13*, 056013. [CrossRef]
6. Bai, Y.; Jin, Y.; Liu, C.; Zeng, Z.; Lian, L. Nezha-F: Design and Analysis of a Foldable and Self-Deployable HAUV. *IEEE Robot. Autom. Let.* **2023**, *8*, 2309–2316. [CrossRef]
7. Jin, Y.; Bi, Y.; Lyu, C.; Bai, Y.; Zeng, Z.; Lian, L. Nezha-IV: A hybrid aerial underwater vehicle in real ocean environments. *J. Field Robot.* **2024**, *41*, 420–442. [CrossRef]
8. Li, L.; Liu, W.; Tian, B.; Hu, P.; Gao, W.; Liu, Y.; Yang, F.; Duo, Y.; Cai, H.; Zhang, Y.; et al. An Aerial–Aquatic Hitchhiking Robot with Remora-Inspired Tactile Sensors and Thrust Vectoring Units. *Adv. Intell. Syst.* **2023**, 2300381. [CrossRef]
9. Liu, X.; Dou, M.; Huang, D.; Gao, S.; Yan, R.; Wang, B.; Cui, J.; Ren, Q.; Dou, L.; Gao, Z.; et al. TJ-FlyingFish: Design and Implementation of an Aerial-Aquatic Quadrotor with Tiltable Propulsion Units. In Proceedings of the 2023 IEEE International Conference on Robotics and Automation (ICRA), London, UK, 26 May–2 June 2023; pp. 7324–7330.
10. Zeng, Z.; Lyu, C.; Bi, Y.; Jin, Y.; Lu, D.; Lian, L. Review of hybrid aerial underwater vehicle: Cross-domain mobility and transitions control. *Ocean Eng.* **2022**, *248*, 110840. [CrossRef]
11. Gnemmi, P.; Changey, S.; Meder, K.; Roussel, E.; Rey, C.; Steinbach, C.; Berner, C. Conception and Manufacturing of a Projectile-Drone Hybrid System. *IEEE/ASME T. Mech.* **2017**, *22*, 940–951. [CrossRef]
12. Zhou, X.; Wen, X.; Wang, Z.; Gao, Y.; Li, H.; Wang, Q.; Yang, T.; Lu, H.; Cao, Y.; Xu, C.; et al. Swarm of micro flying robots in the wild. *Sci. Robot.* **2022**, *7*, eabm5954. [CrossRef] [PubMed]
13. Pastor, D.; Izraelevitz, J.; Nadan, P.; Bouman, A.; Burdick, J.; Kennedy, B. Design of a Ballistically-Launched Foldable Multirotor. In Proceedings of the 2019 IEEE/RSJ International Conference on Intelligent Robots and Systems (IROS), Macau, China, 3–8 November 2019; pp. 5212–5218. [CrossRef]
14. Bouman, A.; Nadan, P.; Anderson, M.; Pastor, D.; Izraelevitz, J.; Burdick, J.; Kennedy, B. Design and Autonomous Stabilization of a Ballistically-Launched Multirotor. In Proceedings of the 2020 IEEE International Conference on Robotics and Automation (ICRA), Paris, France, 31 May–31 August 2020; pp. 8511–8517. [CrossRef]
15. Si, P.; Wu, M.; Huo, Y.; Wu, Z. Investigation of a Tube-Launched Unmanned Aerial Vehicle with a Variable-Sweep Wing. *Drones* **2024**, *8*, 474. [CrossRef]
16. Finigian, M.; Kavounas, P.A.; Ho, I.; Smith, C.C.; Witusik, A.; Hopwood, A.; Avent, C.; Ragasa, B.; Roth, B. Design and Flight Test of a Tube-Launched Unmanned Aerial Vehicle. *Aerospace* **2024**, *11*, 133. [CrossRef]
17. Zhuang, Q.; Zhang, H.; Zhao, C.; He, X.; Liu, Y.; Liu, Z.; Li, S.; Zhu, R.; Wu, D. Effects of the launch parameters on trans-phase stability performance and mechanism for submarine-launched missiles model. *Ocean Eng.* **2023**, *283*, 115083. [CrossRef]
18. Yun, H.; Liu, Q.; Zeng, Z.; Lian, L. Experimental study on water-exit of cylinder. *Ocean Eng.* **2024**, *293*, 116585. [CrossRef]
19. Bi, Y.; Lu, D.; Zeng, Z.; Lian, L. Dynamics and control of hybrid aerial underwater vehicle subject to disturbances. *Ocean Eng.* **2022**, *250*, 110933. [CrossRef]
20. Yuh, J. Design and Control of Autonomous Underwater Robots: A Survey. *Auton. Robots* **2000**, *8*, 7–24. [CrossRef]
21. Liang, C.; Qiao, Z.; Xiang, H.; Yuan, X.; Zheng, X.; Lv, Q. Overall Technology Research of an UAV-Launcher System Based on Electromagnetic Launch. In Proceedings of the 2020 3rd International Conference on Unmanned Systems (ICUS), Harbin, China, 27–28 November 2020; pp. 1196–1199.
22. Gokbel, E.; Gullu, A.; Ersoy, S. Improvement of UAV: Design and implementation on launchability. *Aircr. Eng. Aerosp. Technol.* **2023**, *95*, 734–740. [CrossRef]
23. Zhang, H.; Yang, Y.; Cai, R. Dynamics simulation of folding wing UAVs launched from a high-altitude balloon platform. *Proc. Inst. Mech. Eng. Part G J. Aerosp. Eng.* **2023**, *237*, 3072–3091. [CrossRef]
24. Hu, R.; Lu, D.; Xiong, C.; Lyu, C.; Zhou, H.; Jin, Y.; Wei, T.; Yu, C.; Zeng, Z.; Lian, L. Modeling, characterization and control of a piston-driven buoyancy system for a hybrid aerial underwater vehicle. *Appl. Ocean Res.* **2022**, *120*, 102925. [CrossRef]

25. Fenton, J.D. A Fifth-Order Stokes Theory for Steady Waves. *J. Waterw. Port Coast.* **1985**, *111*, 216–234. [CrossRef]
26. Hirt, C.W.; Nichols, B.D. Volume of fluid (VOF) method for the dynamics of free boundaries. *J. Comput. Phys.* **1981**, *39*, 201–225. [CrossRef]

**Disclaimer/Publisher's Note:** The statements, opinions and data contained in all publications are solely those of the individual author(s) and contributor(s) and not of MDPI and/or the editor(s). MDPI and/or the editor(s) disclaim responsibility for any injury to people or property resulting from any ideas, methods, instructions or products referred to in the content.